Nuclear Science and Techniques (2026) 37:55
https://doi.org/10.1007/s41365-025-01871-5

Deformed shell gap near $N \sim 100$ for Gd and Dy nuclei

S. K. Ghorui[1,2,3] · **A. Ghosh**[4]

Received: 9 December 2024 / Revised: 26 March 2025 / Accepted: 28 April 2025 / Published online: 23 January 2026

Abstract
The structures of even–even Gd and Dy isotopes around $N = 100$ were investigated using a fully self-consistent microscopic model. The systematics of the exited 2_1^+ and 4_1^+ energies reveal a peak-like structure at $N = 100$ along the Gd ($Z = 64$) and Dy ($Z = 66$) isotopic chains. This supports the evidence for a subshell gap near $N = 100$. The nuclear structure properties studied are important to understand the *r*-process elemental abundance peak at $A \sim 160$.

Keywords Nuclear structure · Deformed shell gap · Deformed Hartree–Fock · Angular momentum projection · EM transition

1 Introduction

The study of exotic nuclei, especially nuclei toward the neutron drip line, has opened a new field in the study of the structure of finite quantum mechanical systems. The study of exotic nuclei has revealed novel phenomena that have not been observed in stable nuclei. As we move away from the line of stability toward the dip-lines, traditional spherical shell closures disappear, and deformed shell gaps emerge. The deformed shell gap in single-particle structures stabilizes nuclei with large deformations, similar to spherical shell closures for traditional magic nuclei. The disappearance of the traditional magic numbers and the appearance of new magic numbers [1–5] are evident in lighter mass regions and challenge our understanding of nuclear forces. Such new phenomena in heavier unstable nuclei have gained attention recently, but remain to be thoroughly investigated. The existence of a new neutron shell gap at $N = 100$ has been predicted from mean-field calculations [6–8] and is also evident from experiments [9, 10]. The study of neutron-rich midshell nuclei is relevant to the new shell structure.

The study of neutron-rich nuclei far from the line of β -stability is also important from an astrophysical perspective. Elements heavier than Fe are known to be synthesized by *s*-, *r*- and *p*-processes. The rare-earth nuclei are assumed to be produced via *s*- and *r*-processes. However, the sites for *r*-process are not accurately known. A huge breakthrough was made in 2017, when the Advanced LIGO and Advanced Virgo gravitational-wave detectors discovered a binary neutron star merger named GW170817 [11]. Gravitational-wave observations were followed by the detection of the electromagnetic radiation of GW170817 over a wide range of frequencies. The measurements [12–15] of the afterglow of GW170817 (known as 'kilonova') provided important clues about the synthesis of heavy elements by *r*-process. Other possible candidate sites are neutronized ejecta material from supernova explosions and neutrino-driven wind from a neutron star formed from a type II supernova [16]. The *r*-process abundance distribution has large peaks at $A \sim$ 80, 130, and 195. The neutron shell closures are responsible for the observation of these peaks in the spectrum. This is because closed-shell nuclei have longer beta-decay lifetimes and capture neutrons reluctantly. Therefore, in the *r*-process path, neutron closed-shell nuclei act as waiting points and their abundance increases. This mechanism has been known for several years [17]. The rare-earth region has a small but

✉ S. K. Ghorui
surjakiran@gmail.com

✉ A. Ghosh
anima.ghosh@sru.edu.in

[1] Institute of Modern Physics, Chinese Academy of Sciences, Lanzhou 730000, China

[2] Department of Physics, Vaagdevi Engineering College, Warangal 506005, India

[3] School of Physics and Astronomy, Shanghai Jiao Tong University, Shanghai 200240, China

[4] Department of Physics, School of Sciences and Humanities, Warangal 506371, India

distinct peak at $A \sim 160$. This is known as the rare-earth element (REE) peak. In contrast to the large peaks, the origin of this peak or bump-like structure in the abundance pattern is not clearly understood. Deformation has been suggested to play an important role in the formation of the REE peak [18]. The existence of a deformation maximum can act like a neutron closed shell if the next isotope is less stable for deformation and the binding energy decreases with the addition of a neutron.

The nuclear ground-state quadrupole deformation (β_2) is predicted by the macroscopic-microscopic calculation (finite range droplet model, FRDM) by Möller et al. [19], the relativistic mean-field (RMF) theory by Lalazissis et al. [20], and the Hartree–Fock-BCS+MSk7 (HFBCS) by Goriely et al. [21] and others. Both FRDM and RMF predict the maximum deformation at $N = 102$. However, the HFBCS predicts at $N = 100$. The development of quadrupole deformation and the position of the maximum deformation are not well understood. Experimentally, these lighter rare-earth nuclei with $N = 100$ and beyond have scarcely been studied because of the enormous difficulties.

Here, we theoretically study the systematics of the bulk and microscopic properties of even–even $^{154-170}$Gd and $^{156-172}$Dy rare-earth isotopic chains employing the deformed Hartree–Fock (HF) and angular momentum (J) projection method [22, 23]. Self-consistent microscopic calculations were performed by directly considering the residual interaction. This model with the residual interaction built into the HF states is very close to the shell model as has been shown by earlier studies [24, 25].

2 Deformed Hartree–Fock and angular momentum projection

In this section, we briefly discuss the model for the sake of completeness. The details of the deformed Hartree–Fock and angular momentum projection methods can be found in Refs. [22, 26, 27]. The model (namely DHF model) used by us is based on a quantum many-body method which has been quite successful in explaining the structure of nuclei in the rare-earth region [8, 28–30] as well as lighter mass region [26, 27]. It is based on the deformed Hartree–Fock model for the intrinsic states and angular momentum projection (J-projection, for short) for the physical states, based on these intrinsic states.

This basis is enriched compared to the Nilsson basis because the pp, nn, and pn correlations are built in by the inclusion of residual interaction in a self-consistent manner through the HF iteration procedure. Occupation of the lowest HF orbits by the active neutrons and protons forms the ground band ($K = 0$) intrinsic configuration for even–even nuclei. Here we use an axially symmetric basis with K quantum number for each intrinsic state. This is actually not a limitation of our model because we can diagonalize among various K configurations after J-projection.

An intrinsic wave function $|\phi_K\rangle$ is a superposition of states of good angular momenta:

$$|\phi_K\rangle = \sum_J C_K^J \psi_K^J. \tag{1}$$

One needs to project out states of good angular momenta from the intrinsic state $|\phi_K\rangle$ using the angular momentum projection operator:

$$P_K^{IM} = \frac{2I+1}{8\pi^2} \int \mathrm{d}\Omega D^I_{MK}{}^*(\Omega)\, R(\Omega). \tag{2}$$

Here, $R(\Omega)$ is the rotation operator $e^{-i\alpha J_z}\, e^{-i\theta J_y}\, e^{-i\gamma J_z}$ and Ω represents the Euler's angles α, θ and γ. The Euler's angles α and γ are integrated out because of the axial symmetry, but the remaining one θ has to be integrated numerically. We use 64 point Gauss–Legendre quadrature to evaluate θ integration. It is important to restore rotational symmetry using such a projection operator. The angular-momentum-projected normalized states are given by

$$\Phi_K^{IM} = \frac{P_K^{IM} \mid \phi\rangle}{\sqrt{\langle\phi \mid P_K^{IK} \mid \phi\rangle}}. \tag{3}$$

The energies of the states are obtained from the Hamiltonian overlap given by

$$\langle \Phi^I_{K_2} \mid H \mid \Phi^I_{K_1}\rangle = \frac{2I+1}{2} \frac{1}{(N^I_{K_1K_1} N^I_{K_2K_2})^{1/2}} \int \mathrm{d}\theta \sin\theta d^I_{K_2K_1}(\theta) \langle\phi_{K_2}|He^{-i\theta J_y}|\phi_{K_1}\rangle, \tag{4}$$

with $N^I_{KK} = \langle\phi \mid P_K^{IK} \mid \phi\rangle$. N^I_{KK} represents the intensity of angular momentum I in a K configuration.

In general, two states $|\Phi^{I_1M}_{K_1}\rangle$ and $|\Phi^{I_2M}_{K_2}\rangle$ projected from two intrinsic configurations $|\phi_{K_1}\rangle$ and $|\phi_{K_2}\rangle$ are not orthogonal. We orthonormalize them using the following equation

$$\sum_{K'} (H^I_{KK'} - E_I N^J_{KK'}) b^I_{K'} = 0. \tag{5}$$

Here $N^I_{KK'}$ are amplitude overlap and $b^I_{K'}$ are the orthonormalized amplitudes, which can be identified as band-mixing amplitudes. The orthonormalized states are given by

$$\Psi^{IM} = \sum_K b^I_K \Psi^{IM}_K. \tag{6}$$

With these orthonormalized states, we can calculate matrix elements of various tensor operators.

The reduced matrix element of a tensor operator T^L of polarity L between projected states $\Psi^{I_1}_{K1}$ and $\Psi^{I_2}_{K2}$ is given by

$$\langle \Psi^{I_1}_{K_1} || T^L || \Psi^{I_2}_{K_2} \rangle = \frac{1}{2} \frac{(2I_2+1)(2I_1+1)^{1/2}}{(N^{I_1}_{K_1K_1} N^{I_2}_{K_2K_2})^{1/2}} \sum_{\mu\nu} C^{I_2 L I_1}_{\mu\nu K_1} \int_0^{\pi} \mathrm{d}\theta \sin(\theta) d^{I_2}_{\mu K_2}(\theta) \langle \phi_{K_1} | T^L_\nu e^{-i\theta J_y} | \phi_{K_2} \rangle \ . \tag{7}$$

3 Results and discussions

3.1 Deformation properties

In deformed (axial) Hartree–Fock and angular momentum projection technique [for details see [23, 27] and references therein], we start with a model space and an effective interaction. The model space is presently limited to one major shell for protons and neutrons lying outside the ^{132}Sn core. The $3s_{1/2}$, $2d_{3/2}$, $2d_{5/2}$, $1g_{7/2}$, $1h_{11/2}$, and $1h_{9/2}$ proton states have energies 3.654, 3.288, 0.731, 0.0, 3.205, and 6.96 MeV, and the $3p_{1/2}$, $3p_{3/2}$, $2f_{5/2}$, $2f_{7/2}$, $1h_{9/2}$, and $1i_{13/2}$ neutron states have energies 4.462, 2.974, 3.432, 0.0, 0.686, and 1.487 MeV, respectively [30, 31]. We use surface delta interaction (SDI) [32] as the residual interaction among the active nucleons within the valence space. The strength of the SDI was taken to be 0.3 MeV for p-p, n-n, and p-n interactions in our calculation [28, 33]. The strength was fixed to reproduce relative binding energies of nuclei in the rare-earth mass region [33]. Despite its simplicity, this interaction provides a good description of the systematic deformations in this mass region [33, 34]. Also the interaction reproduces quite well the relative experimental binding energies of the Gd and Dy isotopic chains, respectively [30]. Therefore, despite being a simpler schematic interaction, the SDI is very useful for understanding the simplicity of complex calculations. It can simulate the main important correlations, short range (pairing), and long range (quadrupole) of nuclei in a rather simple way [35, 36]. It is also evident that SDI gives qualitatively the same behavior as the pairing plus quadrupole interaction for the first excited 2^+_1 state in even–even nuclei [37]. The HF calculation for the valence nucleons lying outside the ^{132}Sn core is performed for both prolate and oblate shapes. However, the oblate HF energy lies above (1 MeV or more) the prolate HF ground-state energy for the Gd and Dy isotopic chains. Therefore, we considered the prolate shape as the ground configuration.

As the proton and neutron orbits are filled beyond the closed shell, the deformation and collectivity increase. The maximum deformation was expected at the middle of the shell. The ^{170}Dy isotope with $Z = 66$ and $N = 104$ lies in the middle of the proton shell $Z = 50 - 82$ and neutron shell $N = 82 - 126$. Hence, ^{170}Dy is expected to have the most collective nuclei in its ground state [40]. However, experimental data are not currently available for this isotope. In Fig. 1, we have plotted the quadrupole deformation (β_2) parameters for N=90–106 isotopes of Gd and Dy. Our DHF results for β_2 are compared with available experimental [38, 39] as well as RMF [20], FRDM [19], and HFBCS [21] calculations. All theoretical values, including the DHF results, were slightly lower than the experimental data. However, the overall trends were correctly reproduced. The β_2 values increased steadily with N and were nearly stabilized after $N = 96$, with a maximum at $N \sim 100$. This shows that β_2 value tends to decrease beyond $N = 102$. The quadrupole and hexadecapole moments for the prolate Hartree–Fock solutions are listed in Table 1. From Table 1, we can see that the nuclei studied here possess large static ground-state quadrupole moments.

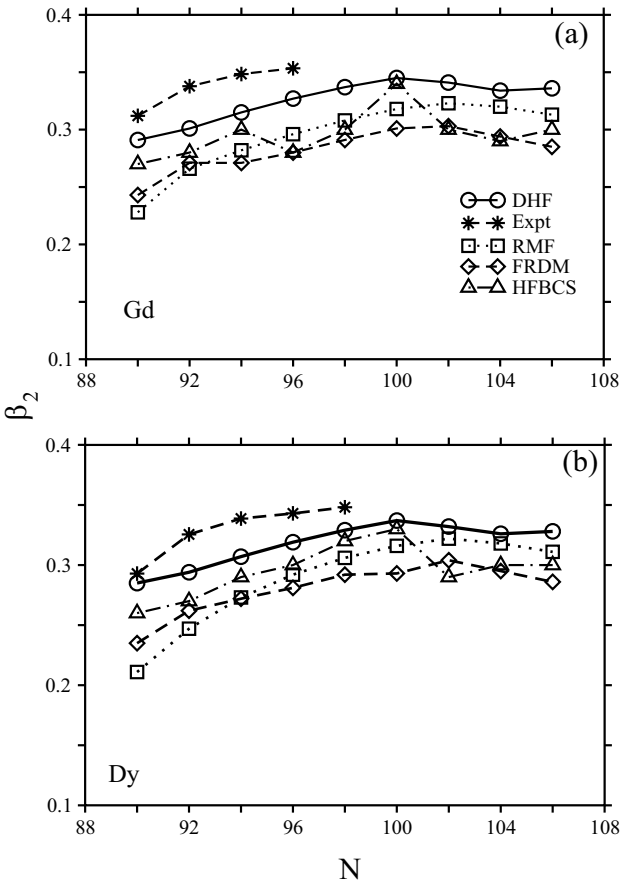

Fig. 1 Quadrupole deformation (β_2) versus neutron number (N) plot for Gd and Dy nuclei. Experimental data are taken from [38, 39]

Table 1 The values of the quadrupole $[Q_2 = \langle r^2 Y_{20}(\theta)\rangle]$ and hexadecapole $[Q_4 = \langle r^4 Y_{40}(\theta)\rangle]$ moments obtained for prolate Hartree–Fock ground states in $^{154-170}$Gd and $^{156-172}$Dy

Z	A	E_{DHF} (MeV)	$B.E.$ (expt) (MeV)	Q_2 [b]		Q_4 [b^2]	
				Proton	Neutron	Proton	Neutron
64	154	−1266.55	−1266.55	13.45	14.34	14.01	41.25
	156	−1280.26	−1281.59	13.57	15.86	13.40	20.78
	158	−1293.77	−1295.88	13.60	18.20	13.68	41.97
	160	−1307.56	−1309.28	13.63	20.27	13.75	54.29
	162	−1320.93	−1321.76	13.70	21.89	13.17	36.25
	164	−1332.94	−1333.32	13.73	23.37	13.00	33.37
	166	−1345.67	−1344.27	13.75	22.86	12.76	12.47
	168	−1357.27	−1354.25	13.75	21.99	12.55	− 10.13
	170	−1369.02	−1362.89(sys)	13.77	22.61	12.17	− 28.98
66	156	−1278.02	−1278.02	13.64	14.54	9.74	41.98
	158	−1292.49	−1294.04	13.75	15.94	9.22	18.43
	160	−1306.97	−1309.45	13.78	18.28	9.56	39.68
	162	−1321.81	−1324.11	13.81	20.35	9.73	52.09
	164	−1336.34	−1338.03	13.87	22.04	9.19	33.10
	166	−1349.04	−1350.79	13.90	23.51	9.10	30.28
	168	−1364.15	−1362.91	13.91	22.98	8.76	9.65
	170	−1377.56	−1374.11	13.92	22.11	8.42	− 12.94
	172	−1391.12	−1384.60	13.94	22.75	8.10	− 31.71

The quantities are given in units of the harmonic oscillator length parameter, $b^2 = 0.9A^{1/3} + 0.7$ fm^2

3.2 Single particle configuration

The prolate-deformed HF single-particle levels for even–even $^{154-170}$Gd and $^{156-172}$Dy are shown in Figs. 2 and 3. The proton and neutron Fermi surfaces are denoted by "dashed" lines, below which the levels are completely filled. The proton single-particle levels remain largely similar throughout the respective isotopic chains both for both Gd and Dy. The neutron single-particle spectra, however, show considerable variation with the change in the valence neutron number, as can be seen from Fig. 2 for the Gd isotopes. It is interesting to note that a considerable gap at the neutron Fermi surface is opened at $N = 100$ isobars compared to its neighboring nuclei. A similar trend

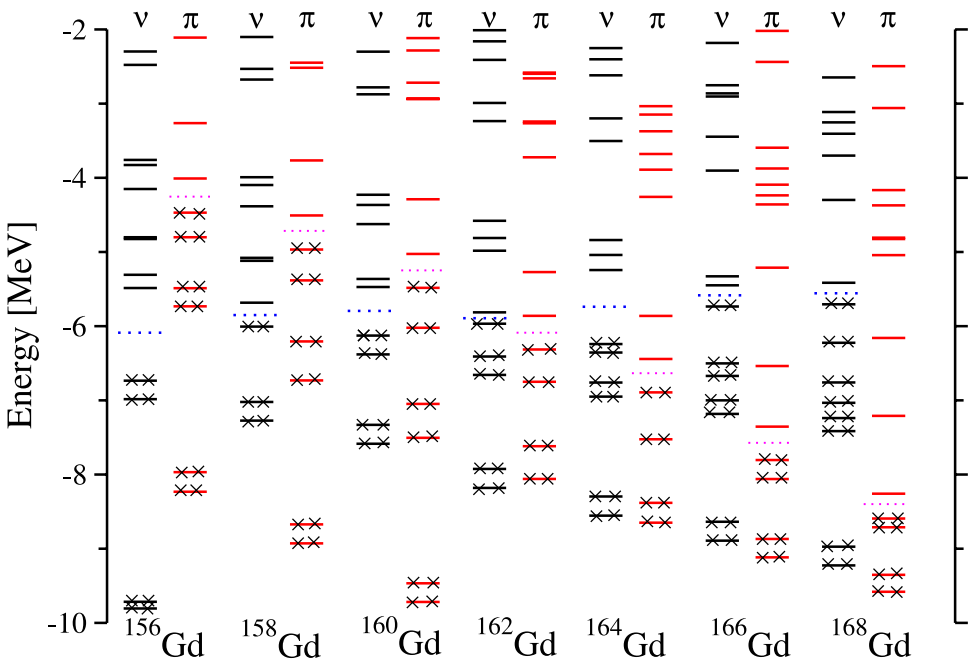

Fig. 2 (Color online) The prolate Hartree–Fock single-particle levels for neutrons (black lines) and protons (red lines) are shown for the Gd isotopic chain. The occupied levels are denoted by '×'. The broken lines guide the eyes to the Fermi surfaces

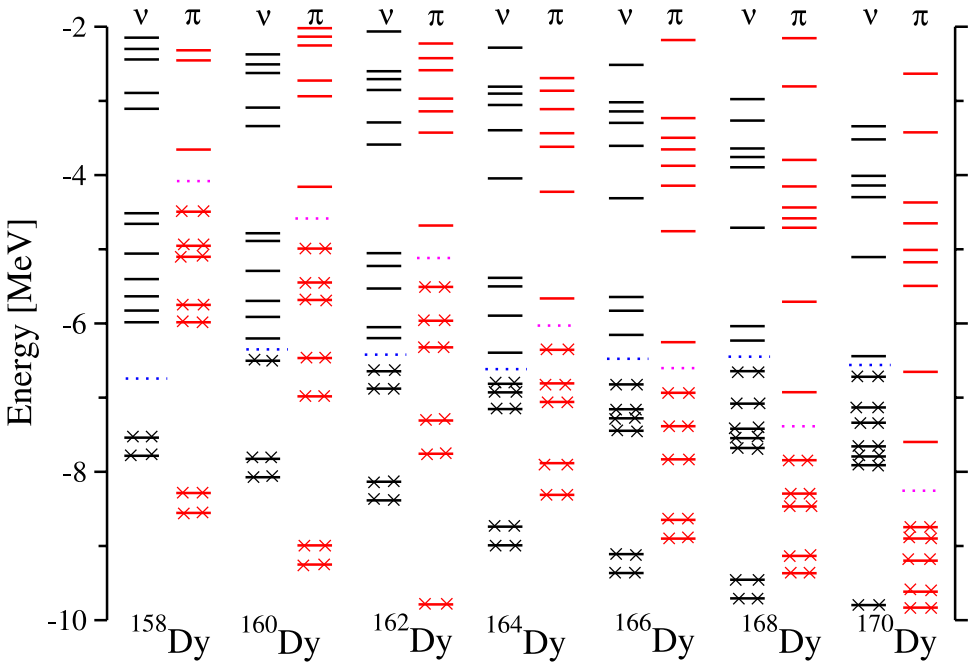

Fig. 3 (Color online) Same as in Fig. 2 but for Dy

was also observed for the nearby $Z = 62$ ^{162}Sm nucleus from the mean-field calculation [33]. The gap in single-neutron levels is prominent for the Gd isotope, whereas it exists for Dy isotopes, but less prominently. This indicates a possible deformed subshell gap near $N = 100$. The possibility of a deformed subshell gap at $N = 100$ for $Z \leq 66$ was also discussed by Patel et al. [9].

The HF single-particle orbits shown in Figs. 2 and 3 are obtained by fully self-consistent deformed HF procedure. We emphasize that the deformation dynamically follows the HF solutions and is not externally imposed. A more familiar Nilsson-like plot can be obtained using constrained HF calculations. However, the HF single-particle levels are largely mixed because of the inclusion of residual interactions during the HF iteration procedure. The components of the single-particle levels can be traced back to each single-particle orbital. To obtain a Nilsson-like deformed single-particle plot, we performed constrained HF calculations. For constrained HF calculation, we use a quadrupole-constrained Hamiltonian given by

$$H'(\lambda) = H - \lambda(Q_{20}^{\mathrm{p}} + Q_{20}^{\mathrm{n}}), \tag{8}$$

with λ being the constraining parameter; Q_{20}^{p} and Q_{20}^{n} are the quadrupole moments of protons and neutrons, respectively. The quadrupole constraint helps to obtain, by a self-consistent procedure, the deformed HF solutions at the desired deformation.

In Fig. 4, we show the Nilsson-like single-particle orbits near the neutron Fermi surface for ^{164}Gd. As mentioned earlier, a considerable gap opens up at the neutron

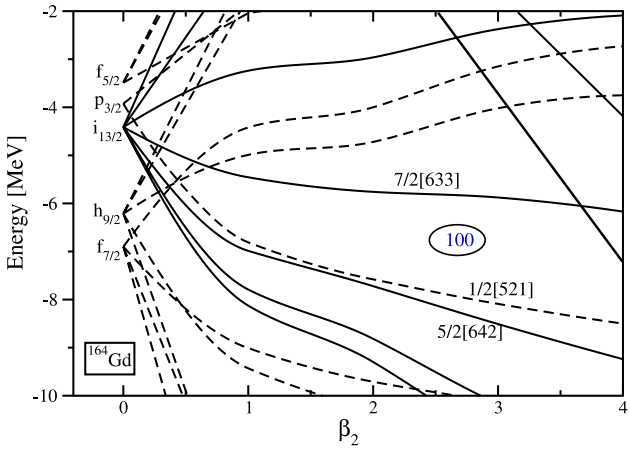

Fig. 4 Nilsson neutron single-particle levels for nuclei near ^{164}Gd

Fermi surface near $N = 100$. Furthermore, higher-order deformations (e.g., β_4, β_6) may influence the size of the gap.

It is to be noted (stressed) that $\langle H \rangle$, the original Hamiltonian (and not the constrained Hamiltonian) is used to evaluate the energy of the systems and other observable quantities presented later in the discussion.

3.3 Systematic of the first 2^+ and 4^+ energies

Figure 5a shows the systematics of the first 2^+ energy $E(2^+)$ for even–even Gd, Dy, and Er rare-earth nuclei. A local maximum at $N = 100$ is evident for the Gd and Dy nuclei and less prominent for the Sm isotope [39]. From

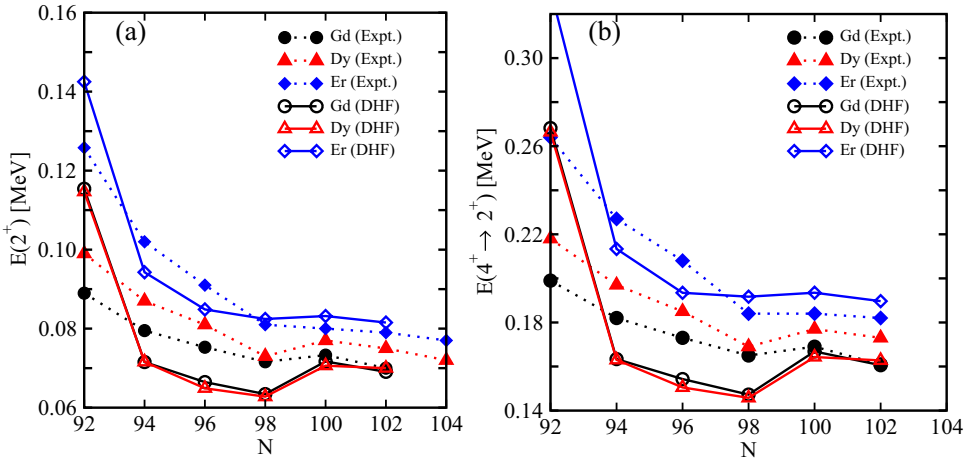

Fig. 5 (Color online) Comparison of theoretical and experimental data for **a** $E(2^+)$ and **b** $E(4^+ \rightarrow 2^+)$. Experimental data are taken from [39, 41–44]

our calculations, we observed a similar trend for the Gd and Dy nuclei, as shown in Fig. 5a. Near $Z = 68$, ^{168}Er does not exhibit such a trend at $N = 100$. The $E(2^+)$ values decrease from $N = 92$ to $N = 98$. From Fig. 5a, it can be seen that the 2^+ energy for $N = 100$ is higher than that of its immediate neighbors. A similar nature is also observed for $N = 100$ and $Z = 62$ isotopes [9]. This supports the possible increase in stability at $N = 100$, $62 \leq Z \leq 66$ nuclei in the rare-earth mass region. Similar to $E(2^+)$, the systematics of $E(4^+ \rightarrow 2^+)$ also show an increase at $N = 100$ for Gd and Dy isotopes, as shown in Fig. 5b. This trend was well reproduced by our DHF calculations. However, the Er isotopic chain does not show such variations, as is evident from the experimental and theoretical data shown in Fig. 5b.

3.4 Electromagnetic properties

Electromagnetic properties (e.g., $B(E2)$, quadrupole, and dipole moments) are very useful tools for testing collectivity in nuclear states, as these quantities are very sensitive to nuclear wave functions. The calculated values are often compared with available experimental data to ensure the wave function reliability. However, the experimental information is limited for most of the nuclei studied here. These nuclei lie close to the drip line, and experiments are difficult to perform, even with sophisticated modern facilities.

The reduced electric quadrupole transition strength $B(E2)$ from an initial state αI_1 to final state βI_2 is given by

$$B(E2;\alpha I_1 \rightarrow \beta I_2) = \frac{1}{(2I_1+1)} \left| \sum_{i=\mathrm{p,n}} \langle \Psi^{\beta I_2}_{K_2} || Q^i_2 || \Psi^{\alpha K I_1}_{K_1} \rangle \right|^2, \quad (9)$$

where $i = \mathrm{p}$ and n are the protons and neutrons, respectively. Here, α and β correspond to two bands that can be the same or different. The summation is for the quadrupole moment operators of the active protons and neutrons. The effective charges for the proton and neutron are taken as $e_\mathrm{p} = 1 + e_\mathrm{eff}$ and $e_\mathrm{n} = e_\mathrm{eff}$ with $e_\mathrm{eff} = (0.5, 0.75)$. The $B(E2;2^+ \rightarrow 0^+)$ values calculated DHF are shown in Figs. 6 and 7 for the Gd and Dy isotopic chains, respectively. The theoretical values were compared with the experimental data whenever available. Experimental data are only available for lighter nuclei in the isotopic chains currently being studied. It can be seen from Figs. 6 and 7 that the experimental values are better reproduced with the effective charges $e_{\mathrm{p(n)}} = 1.75(0.75)$. Although these effective charges are larger compared to the standard values $e_{\mathrm{p(n)}} = 1.5(0.5)$, these values seem to be reasonable as our model space is not too large. The $B(E2)$ values show a gradually increasing trend until $N = 100$ and become nearly constant thereafter for both the Gd and Dy chains. As expected, this trend is similar to that of the quadrupole deformation parameter, as shown earlier. The experimental value for $N = 100$, ^{164}Gd, although has a large

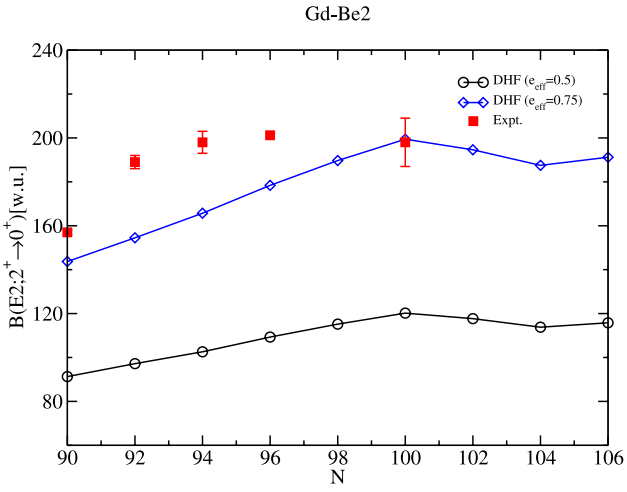

Fig. 6 Comparison of theoretical and experimental data for $E2$ transition probability for even-even $^{154-170}$Gd nuclei. Experimental data are taken from [39, 41–44]

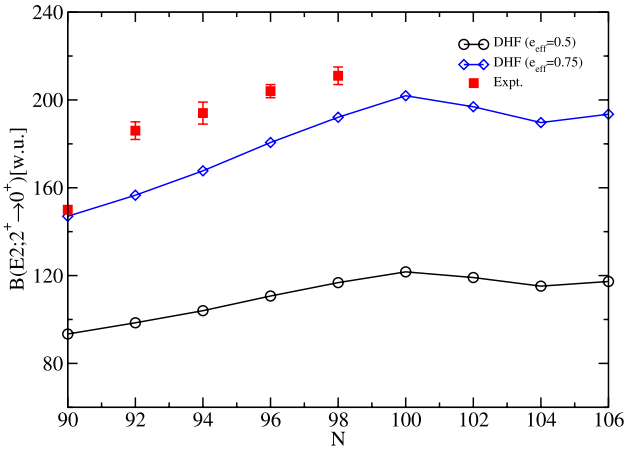

Fig. 7 Comparison of theoretical and experimental data for $E2$ transition probability for even-even $^{156-172}$Dy nuclei. Experimental data are taken from [39, 41–44]

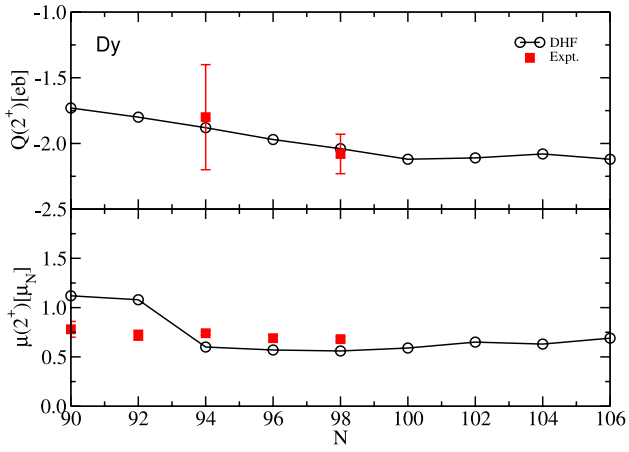

Fig. 9 Same as Fig. 8, but for even–even $^{156-172}$Dy nuclei. Experimental data are taken from [39, 41–44]

uncertainty, well reproduced in our calculations. Beyond $N = 100$, experimental data are not available.

We have also calculated the electric quadrupole moment, Q, and magnetic dipole moment, μ, for the first 2^+ state, as shown in Figs. 8 and 9 for the Gd and Dy isotopic chains. The quadrupole moments were calculated with the effective charges $e_{p(n)} = 1.75(0.75)$. The available experimental data and the trend of quadrupole moments with increasing neutron number (N) were reproduced quite well in our calculations. The experimental values are spare and suffer from large uncertainties for Dy isotopes. The systematic calculation of the quadrupole moments showed a smooth variation with the neutron number (N) throughout the isotopic chains,

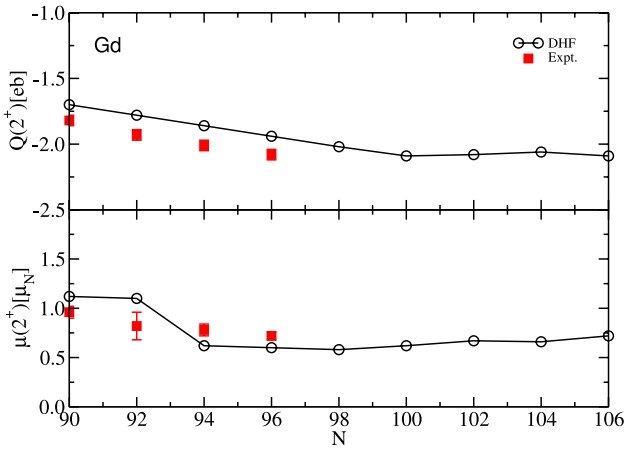

Fig. 8 Comparison of theoretical and experimental data electric quadrupole moment, Q (upper panel), and magnetic dipole moment, μ (lower panel), for the first 2^+ state of even–even $^{154-170}$Gd nuclei. Experimental data are taken from [39, 41–44]

although a minor change is apparent at $N = 100$ for both the Gd and Dy isotopes. To calculate the magnetic dipole moments, we use the g factors $g_l = 1.0\,\mu_N$, $g_s = 5.586 \times 0.75$ μ_N for protons, and $g_l = 0$ μ_N, $g_s = -3.826 \times 0.75$ μ_N for neutrons. A quenching factor of 0.75 for g_s is used to consider the core-polarization effect [45]. The calculated values for $\mu(2^+)$ agree reasonably well with the available experimental results, as shown in the lower panel of Figs. 8 and 9. The dipole moments are not well reproduced for ^{156,158}Dy. One of the reasons for this may be the single-particle energies. At the drip line, neutron single-particle energies are still not well known. The $\nu h_{11/2}$ orbit has a large influence on the g–factor or magnetic moment. Therefore, the different contributions of $\nu h_{11/2}$ in the many-body nuclear wave function can alter the final dipole moment. We have not observed any variation in $\mu(2^+)$ at N=100 for these nuclei.

4 Summary and conclusions

A systematic study of the bulk and microscopic properties and the resulting possible deformed subshell gap around the neutron drip line was carried out for $N = 90 - 102$ isotopes of Gd and Dy. To understand the structure of deformed nuclei, the basis is to study single-particle motion in a deformed potential. The deformed Hartree–Fock theory for the intrinsic structure and angular momentum projection for the restoration of rotational symmetry are useful techniques in such studies. The intrinsic configurations were generated by self-consistent deformed Hartree–Fock calculations, including the effect of residual interaction. The residual interaction causes mixing among the valence nucleons. The deformation follows dynamically based on the deformed HF theory. The intrinsic states are not the physical states of the nuclear system. One needs to do angular

momentum projection to obtain a physical state with good angular momentum.

Our DHF calculations predict a smooth variation in quadrupole deformation with increasing neutron number. The β_2 value reaches a maximum at $N \sim 100$ and nearly stabilizes after that for both the Gd and Dy isotopic chains. The HFBCS+MSk7 [21] calculations show a distinct peak at $N = 100$. The Skyrme Hartree–Fock calculations predict the maximum deformation for Dy isotopes at either $N = 100$ or $N = 102$, depending on the various parameterizations [46]. The FRDM [19] and RMF [20] predict maximum β_2 with smooth variation at $N = 102$ for Sm, Gd and Dy nuclei. Despite the variation in the position of the maximum deformation, all calculations predict that the maximum deformation occurs before $N = 104$ in the neutron midshell.

The systematic $E(2^+)$ energies exhibit a peak-like structure at $N = 100$. This local maximum was also observed in earlier calculations [8] and is evident from experiments [9, 39]. This is an indication of a possible subshell closure at $N = 100$. Recently, it was predicted that the localized maximum deformation and hence the subshell closure may present at $N = 98$ [47]. To understand this result, a recent study modified the standard Nilsson parameters with the introduction of an isotope dependence κ and μ [48]. With this modification, deformed gaps may appear at N=98 or N=100, depending on the isotopes and deformation. An increase in $E(4^+ \rightarrow 2^+)$ at $N = 100$ is also observed and also visible from our calculations, as shown in Fig. 5b. The local maximum for $E(2^+)$ and $E(4^+ \rightarrow 2^+)$ is not present for Er($Z = 68$) at $N = 100$. A deformed shell gap usually manifests a discontinuity in the two-neutron separation energy (S_{2n}) in a manner similar to that of the spherical shell gap, but less prominently. However, no such major changes in S_{2n} are visible for the Dy isotopic chain, where the experimental mass is known [49–51]. For other isotopes, the experimental masses are still unknown. Hence, the masses of these nuclei may be determined using the new generation of experimental facilities.

As the deformation peaks near $N = 100$, we expect similar behavior for $B(E2;2^+ \rightarrow 0^+)$ values. The maximum $B(E2)$ values and hence high collectivity are observed in the present DHF calculations, as shown in Figs. 6 and 7. This may indicate maximum deformation-driven subshell closure at $N = 100$. Although this prediction is not clearly evident from the calculated quadrupole moments, a minor variation in the quadrupole moments at $N = 100$ indicates a change in the shell structure.

From our self-consistent microscopic calculations, a deformation maximum at $N = 100$ was observed, which may act like a subshell closure for $62 \leq Z \leq 66$ nuclei. This gap influenced the *r*-process abundance peak at $A \sim 160$. However, experimental data on these drip-line nuclei are still insufficient. Further experimental and theoretical investigations are required. Because of ambiguities regarding the single-particle energies in neutron drip-line nuclei, it is necessary to study the deformed Nilsson levels in these areas of the nuclear chart. In particular, their variations have higher-order deformations (e.g., β_3, β_4, β_6). All of these are planned for future studies in a systematic way.

Acknowledgements The authors, especially SKG, acknowledge Prof. Y. Sun and Prof. S. K. Patra for their fruitful discussions and suggestions for the present work. SKG acknowledges the support of IOP Bhubaneswar during his visit. AG acknowledges the support of SR University.

Author Contributions All authors contributed to the study conception and design. Material preparation, data collection and analysis were performed by all authors. The first draft of the manuscript was written by SKG and AG. All authors commented on previous versions of the manuscript. All authors read and approved the final manuscript.

Declarations

Conflict of interest The authors declare that they have no Conflict of interest.

References

1. R.V.F. Janssens, Nuclear physics: unexpected doubly magic nucleus. Nature (London) **459**, 1069–1070 (2009). https://doi.org/10.1038/4591069a
2. D. Steppenbeck, S. Takeuchi, N. Aoi et al., Evidence for a new nuclear 'magic number' from the level structure of ^{54}Ca. Nature (London) **502**, 207–210 (2013). https://doi.org/10.1038/nature12522
3. M. Brack, J. Damgaard, A.S. Jensen et al., Funny hills: the shell-correction approach to nuclear shell effects and its applications to the fission process. Rev. Mod. Phys. **44**, 320–405 (1972). https://doi.org/10.1103/RevModPhys.44.320
4. M. Rosenbusch, P. Ascher, D. Atanasov et al., Probing the N =32 shell closure below the magic proton number Z =20: mass measurements of the exotic isotopes ^{52,53}K. Phys. Rev. Lett. **114**, 202501 (2015). https://doi.org/10.1103/PhysRevLett.114.202501
5. A. Ozawa, T. Kobayashi, T. Suzuki et al., New magic number, N = 16, near the neutron drip line. Phys. Rev. Lett. **84**, 5493–5495 (2000). https://doi.org/10.1103/PhysRevLett.84.5493
6. L. Satpathy, S. Patra, New magic numbers and new islands of stability in drip-line regions in mass model. Nucl. Phys. A **722**, C24–C29 (2003). https://doi.org/10.1016/S0375-9474(03)01330-7
7. L. Satpathy, S.K. Patra, Shell overcomes repulsive nuclear force instability. J. Phys. G Nucl. Part. Phys. **30**, 771 (2004). https://doi.org/10.1088/0954-3899/30/6/007
8. S.K. Ghorui, B.B. Sahu, C.R. Praharaj et al., Examining the stability of Sm nuclei around $N = 100$. Phys. Rev. C **85**, 064327 (2012). https://doi.org/10.1103/PhysRevC.85.064327
9. Z. Patel, P.A. Söderström, Z. Podolyák et al., Isomer decay spectroscopy of ^{164}Sm and ^{166}Gd: midshell collectivity around N = 100. Phys. Rev. Lett. **113**, 262502 (2014). https://doi.org/10.1103/PhysRevLett.113.262502
10. L.S. Danu, D.C. Biswas, A. Saxena et al., Fine structure dips in the fission fragment mass distribution for the ^{238}U(^{18}O,f) reaction. Phys. Rev. C **81**, 014311 (2010). https://doi.org/10.1103/PhysRevC.81.014311

11. B.P. Abbott, R. Abbott, T.D. Abbott et al., GW170817: observation of gravitational waves from a binary neutron star inspiral. Phys. Rev. lett. **119**, 161101 (2017). https://doi.org/10.1103/PhysRevLett.119.161101
12. D.A. Coulter, R.J. Foley, C.D. Kilpatrick et al., Swope supernova survey 2017a (SSS17a), the optical counterpart to a gravitational wave source. Science **358**, 1556–1558 (2017). https://doi.org/10.1126/science.aap9811
13. S. Valenti, D.J. Sand, S. Yang et al., The discovery of the electromagnetic counterpart of GW170817: Kilonova AT 2017gfo/DLT17ck. Astrophys. J. **848**, L24 (2017). https://doi.org/10.3847/2041-8213/aa8edf
14. M.R. Drout, A.L. Piro, B.J. Shappee et al., Light curves of the neutron star merger GW170817/SSS17a: implications for r-process nucleosynthesis. Science **358**, 1570–1574 (2017). https://doi.org/10.1126/science.aaq0049
15. D. Kasen, B. Metzger, J. Barnes et al., Origin of the heavy elements in binary neutron-star mergers from a gravitational-wave event. Nature **551**, 80–84 (2017). https://doi.org/10.1038/nature24453
16. C. Iliadis, *Nuclear Physics of Stars* (Wiley-VCH Verlag, Weinheim, 2007). https://doi.org/10.1002/9783527692668
17. E.M. Burbidge, G.R. Burbidge, W.A. Fowler et al., Synthesis of the elements in stars. Rev. Mod. Phys. **29**, 547–650 (1957). https://doi.org/10.1103/RevModPhys.29.547
18. R. Surman, J. Engel, J.R. Bennett et al., Source of the rare-earth element peak in *r*-process nucleosynthesis. Phys. Rev. Lett. **79**, 1809–1812 (1997). https://doi.org/10.1103/PhysRevLett.79.1809
19. P. Möller, J.R. Nix, W.D. Myers et al., Nuclear ground-state masses and deformations. Atom. Data Nucl. Data Tabl. **59**, 185 (1995). https://doi.org/10.1006/adnd.1995.1002
20. G.A. Lalazissis, S. Raman, P. Ring, Ground-State properties of even-even nuclei in the relativistic mean-field theory. Atom. Data Nucl. Data Tabl. **71**, 1 (1999)
21. S. Goriely, F. Tondeur, J.M. Pearson, A HARTREE-FOCK nuclear mass table. Atom. Data Nucl. Data Tabl. **77**, 311–381 (2001). https://doi.org/10.1006/adnd.2000.0857
22. G. Ripka, The Hartree-Fock theory of deformed light nuclei. In: Baranger, M., Vogt, E. (eds) Advances in Nuclear Physics. Springer, Boston, MA. https://doi.org/10.1007/978-1-4757-0103-6_3
23. C.R. Praharaj, Study of rotation-alignment in the backbend region by angular momentum projection. Phys. Lett. B **119**, 17–20 (1982). https://doi.org/10.1016/0370-2693(82)90233-7
24. M. Macfarlane, A. Shukla, Shape mixing and the shell-model description of the isotopes of neon. Phys. Lett. B **35**, 11–15 (1971). https://doi.org/10.1016/0370-2693(71)90426-6
25. S.B. Khadkikar, S.C.K. Nair, S.P. Pandya, Shape mixing in ^{24}Ne. Phys. Lett. B **36**, 290–292 (1971). https://doi.org/10.1016/0370-2693(71)90705-2
26. C.R. Praharaj, Structure of krypton nuclei and the low-lying positive parity bands in ^{82}Kr. J. Phys. G Nucl. Phys. **14**, 843–856 (1988). https://doi.org/10.1088/0305-4616/14/7/005
27. S.K. Ghorui, P.K. Raina, A.K. Singh, et al., Study of energy spectra and electromagnetic moments of double beta decay nuclei in deformed Hartree-Fock model. arXiv:1111.1174
28. A.K. Rath, C.R. Praharaj, S.B. Khadkikar, Signature effects in some N=90 odd-Z rare-earth nuclei. Phys. Rev. C **47**, 1990–2000 (1993). https://doi.org/10.1103/PhysRevC.47.1990
29. S.K. Ghorui, C.R. Praharaj, P.K. Raina et al., Energy spectra and electromagnetic transition rates of ^{160,162,164}Gd in the projected Hartree-Fock model. AIP Conf. Proc. **1609**, 135–141 (2014). https://doi.org/10.1063/1.4893266
30. S.K. Ghorui, C.R. Praharaj, Systematic study of high-K isomers in the midshell Gd and Dy nuclei. Eur. Phys. J. A **54**, 163 (2018). https://doi.org/10.1140/epja/i2018-12596-0
31. S. Kahana, H.C. Lee, C.K. Scott, Effect of woods-saxon wave functions on the calculation of $A = 18, 206, 210$ spectra with a realistic interaction. Phys. Rev. **180**, 956–966 (1969). https://doi.org/10.1103/PhysRev.180.956
32. A. Faessler, A. Plastino, S.A. Moszkowski, Surface delta interaction in deformed nuclei. Phys. Rev. **156**, 1064–1071 (1967). https://doi.org/10.1103/PhysRev.156.1064
33. S.K. Ghorui, P.K. Raina, P.K. Rath et al., Rotational bands and electromagnetic transitions of some even-even neodymium nuclei in projected Hartree-Fock model. Int. J. Mod. Phys. E **21**, 50070 (2012). https://doi.org/10.1142/S021830131250070X
34. C.R. Praharaj, S.K. Patra, R.K. Bhowmik et al., Band structures and deformations of rare-earth nuclei. J Phys. Conf. Seri. **312**, 092052 (2011)
35. I.M. Green, S.A. Moszkowski, Nuclear coupling schemes with a surface delta interaction. Phys. Rev. **139**, 790–793 (1965). https://doi.org/10.1103/PhysRev.139.B790
36. M. Baranger, K. Kumar, Nuclear deformations in the pairing-plus-quadrupole model: (I). The single- j shell. Nucl. Phys. **62**, 113–132 (1965). https://doi.org/10.1016/0029-5582(65)90074-X
37. J. Touchard, A connection between the surface delta interaction and the pairing plus quadrupole model in spherical nuclei. Phys. Lett. **21**, 85–86 (1966). https://doi.org/10.1016/0031-9163(66)91352-7
38. S. Raman, C.W.G. Nestor Jr., P. Tikkanen, Transition probability from the ground to the first- excited 2+ state of even-even nu clides. Atom. Data Nucl. Data Tabl. **78**, 1–128 (2001)
39. ENSDF Database [http://www.nndc.bnl.gov/ensdf]. http://www.nndc.bnl.gov/ensdf
40. P.H. Regan, F.R. Xu, P.M. Walker et al., Structure of the doubly midshell nucleus $^{170}_{66}Dy_{104}$. Phys. Rev. C **65**, 037302 (2002). https://doi.org/10.1103/PhysRevC.65.037302
41. B. Singh, J. Chen, Nuclear data sheets for A=164. Nucl. Data Sheets **147**, 1–381 (2018). https://doi.org/10.1016/J.NDS.2018.01.001
42. C.M. Baglin, Nuclear data sheets for $A = 166$. Nucl. Data Sheets **109**, 1103–1382 (2008). https://doi.org/10.1016/J.NDS.2008.04.001
43. C.M. Baglin, Nuclear data sheets for $A = 168$. Nucl. Data Sheets **111**, 1807–2080 (2010). https://doi.org/10.1016/J.NDS.2010.07.001
44. C.M. Baglin, Nuclear data sheets for $A = 170$. Nucl. Data Sheets **96**, 611–873 (2002). https://doi.org/10.1006/NDSH.2002.0015
45. B. Castel, I. Towner, *Modern Theories of Nuclear Moments*, Oxford studies in nuclear physics, (Clarendon Press, 1990)
46. A.K. Rath, P.D. Stevenson, P.H. Regan et al., Self-consistent description of dysprosium isotopes in the doubly Midshell region. Phys. Rev. C **68**, 044315 (2003). https://doi.org/10.1103/PhysRevC.68.044315
47. D.J. Hartley, F.G. Kondev, R. Orford et al., Masses and β-decay spectroscopy of neutron-rich odd-odd ^{160,162}Eu nuclei: evidence for a subshell gap with large deformation at $N = 98$. Phys. Rev. Lett. **120**, 182502 (2018). https://doi.org/10.1103/PhysRevLett.120.182502
48. Y.X. Liu, C.J. Lv, Y. Sun et al., Changes of deformed shell gaps at $N \sim 100$ in light rare-earth, neutron-rich nuclei. J. Phys. G Nucl. Part. Phys. **47**, 055108 (2020). https://doi.org/10.1088/1361-6471/ab752d
49. M. Wang, G. Audi, F. Kondev et al., The ame2016 atomic mass evaluation (II). Tables, graphs and references. Chin. Phys. C **41**, 030003 (2017)

50. M. Vilen, J.M. Kelly, A. Kankainen et al., Precision mass measurements on neutron-rich rare-earth isotopes at JYFLTRAP: reduced neutron pairing and implications for *r*-process calculations. Phys. Rev. Lett. **120**, 262701 (2018). https://doi.org/10.1103/PhysRevLett.120.262701
51. R. Orford, N. Vassh, J.A. Clark et al., Precision mass measurements of neutron-rich neodymium and samarium isotopes and their role in understanding rare-earth peak formation. Phys. Rev. Lett. **120**, 262702 (2018). https://doi.org/10.1103/PhysRevLett.120.262702